

# **Topology-Preserving Scalar Field Optimization for Boundary-Conforming Spiral Toolpaths on Multiply Connected Freeform Surfaces**

Changqing Shen

State Key Laboratory of Intelligent Manufacturing Equipment and Technology, School of Mechanical Science and Engineering, Huazhong University of Science and Technology, Wuhan, 430074, China, d202280361@hust.edu.cn

Bingzhou Xu

State Key Laboratory of Intelligent Manufacturing Equipment and Technology, School of Mechanical Science and Engineering, Huazhong University of Science and Technology, Wuhan, 430074, China, joyeuxxu@hust.edu.cn

Bosong Qi

State Key Laboratory of Intelligent Manufacturing Equipment and Technology, School of Mechanical Science and Engineering, Huazhong University of Science and Technology, Wuhan, 430074, China, poisson\_bs@hust.edu.cn

Xiaojian Zhang\*

State Key Laboratory of Intelligent Manufacturing Equipment and Technology, School of Mechanical Science and Engineering, Huazhong University of Science and Technology, Wuhan, 430074, China, xjzhang@hust.edu.cn

Sijie Yan

State Key Laboratory of Intelligent Manufacturing Equipment and Technology, School of Mechanical Science and Engineering, Huazhong University of Science and Technology, Wuhan, 430074, China, sjyan@hust.edu.cn

Han Ding

State Key Laboratory of Intelligent Manufacturing Equipment and Technology, School of Mechanical Science and Engineering, Huazhong University of Science and Technology, Wuhan, 430074, China, dinghan@hust.edu.cn

---

\* Xiaojian Zhang, State Key Laboratory of Intelligent Manufacturing Equipment and Technology, School of Mechanical Science and Engineering, Huazhong University of Science and Technology, No. 1307, Luoyu Street, Hongshan District, Wuhan, 430074, China. E-mail: xjzhang@hust.edu.cn

**Abstract:**

Ball-end milling path planning on multiply connected freeform surfaces is pivotal for high-quality and efficient machining of components in automotive and aerospace manufacturing. Although scalar-field-based optimization provides a unified framework for multi-objective toolpath generation, maintaining boundary conformity while eliminating zero-gradient singularities that cause iso-curve branching or termination and disrupt toolpath continuity remains challenging on multiply connected surfaces. We propose an efficient strategy to robustly enforce these constraints throughout optimization. Conformal slit mapping is employed to construct a feasible, singularity-free initial scalar field. The optimization is reformulated as a topology-preserving mesh deformation governed by boundary-synchronous updates, enabling globally optimized spacing, scallop-height uniformity, and smooth trajectory transitions. Consequently, the toolpaths are continuous, boundary-conforming, and free of self-intersections. Milling experiments demonstrate that, compared with a state-of-the-art conformal slit mapping-based method, the proposed approach increases machining efficiency by 14.24%, improves scallop-height uniformity by 5.70%, and reduces milling impact-induced vibrations by over 10%. The strategy offers broad applicability in high-performance machining scenarios.

CCS CONCEPTS • Computer-aided design • Computer graphics • Parametric curve and surface models

**Additional Keywords and Phrases:** Spiral Tool Trajectory Planning, Scalar field optimization, Conformal Slit Mapping, Freeform Surface Toolpath Planning

## 1 INTRODUCTION

### Problem Description

In modern manufacturing, component geometries have become increasingly complex, particularly in the automotive and aerospace sectors [Dutra Pereira et al. 2025; Mali et al. 2021; Marin et al. 2025]. Machining quality and efficiency are strongly dependent on the rationality of the toolpath planning. A representative example is an automotive headlamp mold (Figure. 1), whose machined surface contains multiple protrusions. These geometric features obstruct continuous toolpath coverage, causing conventional planning methods to generate five retractions and numerous sharp turns. These path characteristics tend to induce surface defects and reduce machining efficiency. Studies have examined the adverse machining consequences induced by unfavorable toolpath characteristics. For instance, intermittent tool–workpiece separation and re-engagement can lead to fluctuations in material removal [Yan et al. 2019; Yang et al. 2024] and burr formation [Chen et al. 2021]; frequent steering operations may trigger actuator deceleration [Kim and Choi 2002] and intensified vibrations [Wang et al. 2025]; toolpaths that do not conform to surface boundaries tend to leave residual material [Yang et al. 2023]; and self-intersecting trajectories can distort the milling load and cause surface scratching on the machined workpiece [Hajdu et al. 2025].

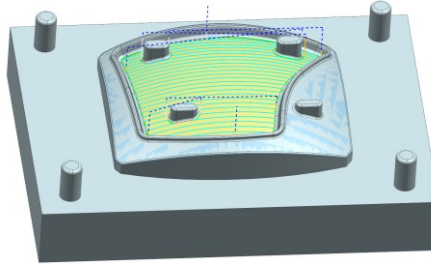


Figure 1: Toolpaths generated for freeform surface machining using commercial CAD/CAM software.

To satisfy the requirements of advanced complex components for both high efficiency and high quality, toolpath planning should minimize path length, interruptions, sharp turns, and self-intersections while enhancing smoothness, scallop-height uniformity, and strict conformity to machining surface boundaries. However, these objectives are often mutually conflicting, which renders their simultaneous achievement within a unified global framework particularly challenging.

### Related work

Based on current knowledge, milling toolpath planning methods for multiply connected surfaces can be broadly classified into three categories: element decomposition [Acar et al. 2003; Choi 2021; Ge et al. 2024; Held and de Lorenzo 2018; Lin et al. 2017; Sun et al. 2016; Wu et al. 2019; Xu et al. 2022], boundary offsetting [Lee 2003; Xu et al. 2019; Zhao et al. 2024; Zhuang et al. 2010], and scalar/vector field optimization [Bartoň et al. 2021; Dutta et al. 2023; Goes et al. 2016; Shen et al. 2024; Shen et al. 2025; Zou 2021; Zou et al. 2014]. In addition, several complete coverage trajectory planning methods have been proposed but are rarely adopted in milling applications because of excessive turning angles, incomplete coverage, and frequent self-intersections [Ban et al. 2013; Song and Gupta 2018]; therefore, they are not discussed in this paper. The first category decomposes complex surfaces into multiple simpler subregions that can be more easily parameterized and are typically assumed to be connected. For example, Acar et al. [2003] divided complex regions by identifying critical boundary points and sweep lines, allowing each subregion to be fully covered by sweep paths. Yu-Yao Lin et al. [2017] employed holomorphic quadratic differentials to decompose a genus- $g$  surface into 3g-3 hole-free subregions, each filled with zigzag coverage paths. Other studies have introduced artificial cutting boundaries to transform multiply connected domains into single or multiple disk- or annulus-like subregions [Sun et al. 2016], within which conformal mapping [Choi 2021] or medial-axis-transform (MAT)-based methods [Ge et al. 2024; Held and de Lorenzo 2018] were adopted to generate spiral or zigzag paths. However, for highly perforated surfaces, such decomposition is often nontrivial and can lead to excessive bridging or severe non-uniformity in path spacing.

The second category is based on boundary offsetting. Lee et al. [2003] proposed an equal-scallop-height offsetting method to generate spiral paths on hole-free surfaces. Xu et al. [2019] computed equal-scallop-height offsets on flattened surfaces using mapping stretch factors, achieving the improved smoothness compared with Lee’s method. Nevertheless, both approaches suffer from sharp turning angles and fragmented paths caused by self-intersections induced by trajectory offsetting. Zhao et al. [2024] extracted sharp-turning regions from offset paths and filled them with zigzag patterns to improve the spacing uniformity, at the cost of increased turns and interruptions. Zhuang et al. [2010] formulated the offsetting process using the level-set evolution, which enabled the smoothness control, while on multiply connected surfaces, the level sets tend to fragment, necessitating additional path bridging.

Regardless of whether decomposition- or offsetting-based strategies are adopted, existing methods frequently generate toolpaths with interruptions, sharp turning angles, and insufficient boundary conformity when holes and protrusions are present. These limitations inevitably degrade machining quality and efficiency, highlighting the need for new toolpath planning approaches capable of producing continuous, smooth, and fully boundary-conforming trajectories on complex multiply connected surfaces.

Recently, scalar/vector field optimization methods [Bartoň et al. 2021; Dutta et al. 2023; Goes et al. 2016; Shen et al. 2024; Shen et al. 2025; Zou 2021; Zou et al. 2014] have emerged as promising alternatives because they provide a global optimization framework that simultaneously accounts for path spacing uniformity, smoothness, and boundary conformity.

Zou et al. [2014] and Zou [2021] redesigned the toolpath planning on hole-free surfaces as a functional optimization problem by constructing a multi-objective energy function to optimize scalar-field isoparametric lines. By enforcing nonzero gradients in the scalar field [Mitra et al. 2024] and fixed isovalues along the boundaries, their method generated isoparametric lines forming a singularity-free foliation [Campen et al. 2016; Vekhter et al. 2019; Zhang et al. 2006] that strictly conformed to surface boundaries, avoided self-intersections and discontinuities, and enabled smooth bridging into a single continuous trajectory for full coverage. However, maintaining a nonzero gradient in numerical implementations remains challenging [Li et al. 2006; Makhanov 2022; Wu et al. 2024], and the optimization of scalar fields on porous surfaces under simultaneous boundary and gradient constraints requires further investigation.

Building on this concept, Shen et al. [2024, 2025] employed conformal slit mapping [Li and Lu 2025; Nasser 2011; Wu and Lu 2023] to construct scalar fields with nonzero gradients and fixed boundary isovalues on multiply connected surfaces. This mapping transformed a complex, multiply connected surface into a simply connected disk or annulus, in which internal holes were mapped to circular arcs, thereby facilitating the construction of scalar fields that satisfied the prescribed dual constraints. Under these constraints, spiral trajectories derived from the scalar field remained continuous, boundary-conforming, and smoothly bridged, whereas the rigid nature of conformal slit mapping can inherently restrict the freedom of subsequent optimization.

Hao et al. [2025] introduced a physics-informed neural network (PINN) to optimally partition surfaces and generate toolpaths guided by a multi-objective scalar field loss function. Chen et al. [2025] further incorporated actuator dynamic characteristics into the scalar-field loss formulation. In addition, M. Bartoň et al. [2021] evaluated the potential interference between non-spherical tools and the workpiece surface using a wedge diagram and incorporated an interference-avoidance term into the scalar-field energy function. The resulting optimal scalar field, solved via TensorFlow, enabled multi-objective optimization that simultaneously avoided tool interference, ensured scallop-height uniformity, and improved toolpath fairness.

These neural network-driven techniques have shown promise in addressing the nonlinear functional optimization of complex scalar fields. However, to the best of our knowledge, they still suffer from poor convergence under complex boundary conditions and incur substantial computational costs [Grossmann et al. 2024]. For instance, when surface contain first-order discontinuities boundaries or internal holes, strict boundary conformity requires scalar fields with derivative discontinuous behavior near the boundaries. Recent studies [Della Santa and Pieraccini 2023; Rahaman et al. 2019] have suggested that neural networks exhibit a low-frequency bias towards smooth approximations, which limits their accuracy in representing such discontinuous functions.

In addition, early work by E. Bohez et al. [2000] proposed a functional optimization objective emphasizing global scallop-height uniformity and toolpath smoothness. However, it did not establish an explicit relationship between multiple optimization objectives and the local differential geometric properties of the scalar field on the surface. Consequently, the method was restricted to quadrilateral-meshed Coons surfaces and did not support adaptive path refinement.

In summary, scalar-field optimization methods for toolpath planning enable multi-objective consideration within a global optimization framework. Nevertheless, effectively optimizing scalar fields on multiply connected surfaces under nonzero-gradient constraints while maintaining strict boundary conformity to further improve path quality remains a significant challenge.

## Our Contribution

In our study, a scalar-field-based functional optimization method was developed for multiply connected surfaces to generate globally optimized spiral toolpaths. The resulting paths exhibited uninterrupted continuity, strict boundary conformity, smooth turning transitions, and uniform scallop height. These capabilities were achieved through two technical contributions.

1. A conformal slit mapping was employed to construct an initial scalar field that satisfied the prescribed dual constraints of boundary conformity and nonzero gradients while remaining close to the optimal solution. This initialization ensured that the optimization began from a constraint-compliant, near-optimal state and substantially reduced the computational cost by avoiding invalid iterations.
2. The iteration of the scalar field on the mesh transitions from updating the scalar values at the mesh vertices to optimizing the mesh morphology. Mesh morphology constraints are imposed to strictly eliminate internal singularities and ensure uniform boundary values of the scalar field, thus preserving the boundary adherence, continuity and non-self-intersection of the scalar field's isoparametric lines during iterative optimization.

## 2 METHOD

### 2.1 Level Set Path of the Scale Field Evaluation Criteria

A scalar field  $T$  is assumed to be defined on the surface  $S$ , and the level sets of  $T$  are assumed to be utilized as milling toolpaths. Following the approach in reference [Rusinkiewicz 2004; Zou et al. 2014], the generated toolpaths were evaluated in terms of scallop-height uniformity and trajectory smoothness, which provided quantitative metrics serving as the optimization objectives for subsequent trajectory refinement. The uniformity of the toolpath scallop height was also assessed.

As shown in Figures 2(a) and 2(b), let  $P_i$  and  $P_{i+1}$  denote two adjacent cutter contact points on the surface  $S$ . They lie on two adjacent isoparametric lines of the scalar field  $T$ , denoted as  $CL_i = \{P \in S | T(P) = T_i\}$  and  $CL_{i+1} = \{P \in S | T(P) = T_{i+1}\}$ , respectively. The corresponding ball-end mill centers were offset from the surface along the normal direction by  $K_c$ , where  $K_c$  is the radius of the ball-end mill. The machining scallop height between  $P_i$  and  $P_{i+1}$  can be expressed as follows:

$$h = \frac{K_s + K_c}{8} \left\| \overrightarrow{P_i P_{i+1}} \right\|_2^2 + o \left( \left\| \overrightarrow{P_i P_{i+1}} \right\|_2^3 \right) \quad (1)$$

where  $K_s$  denotes the normal curvature of the surface  $S$  at  $P_i$  in the direction of  $\overrightarrow{P_i P_{i+1}}$ , and  $\overrightarrow{P_i P_{i+1}}$  is the vector between  $P_i$  and  $P_{i+1}$  (Figure 2(b)). The notation  $o \left( \left\| \overrightarrow{P_i P_{i+1}} \right\|_2^3 \right)$  represents the cubic infinitesimal of the Euclidean norm of  $\overrightarrow{P_i P_{i+1}}$ .

When  $P_{i+1}$  is sufficiently close to  $P_i$ , the direction of  $\overrightarrow{P_i P_{i+1}}$  aligns with the gradient of  $T$  at  $P_i$ , which can be denoted as  $\nabla T(P_i)$ . According to Taylor's theorem, the following equation can be derived:

$$(\| \nabla T(P_i) \|_2) \left( \left\| \overrightarrow{P_i P_{i+1}} \right\|_2 \right) + o \left( \left\| \overrightarrow{P_i P_{i+1}} \right\|_2^2 \right) = |T_{i+1} - T_i| \quad (2)$$

By neglecting higher-order infinitesimals and combining Equations (1) and (2), the following equation can be obtained:

$$h = |T_{i+1} - T_i|^2 \frac{K_s + K_c}{8\|\nabla T(P_i)\|_2^2} \quad (3)$$

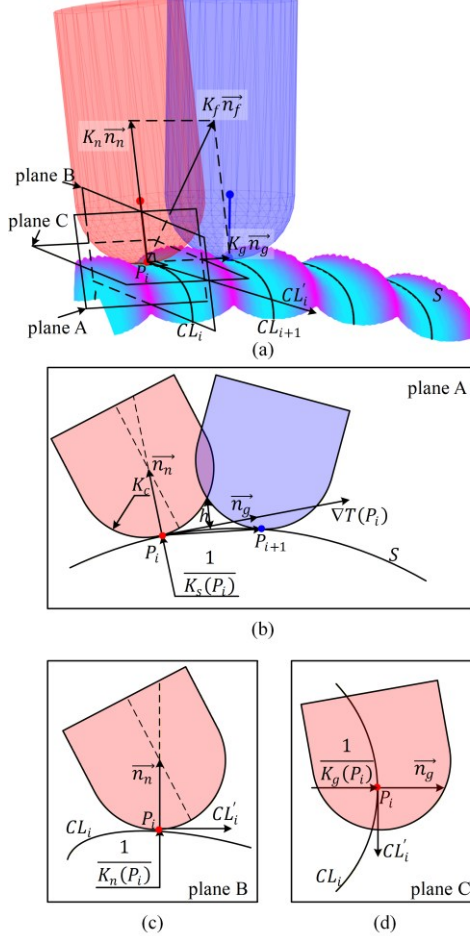


Figure 2: Relationship among  $CL_i$ ,  $CL_{i+1}$ ,  $h$ ,  $\nabla T(P_i)$ ,  $K_s$ ,  $K_c$ ,  $K_f$ ,  $K_n$ , and  $K_g$ .

Because  $|T_{i+1} - T_i|^2$  is constant, it follows from Equation (3) that the variation in the machining height between adjacent isocurves can be characterized by the changes in  $\frac{K_s + K_c}{8\|\nabla T\|_2^2}$ . The average value  $Avg$  of  $\frac{K_s + K_c}{8\|\nabla T\|_2^2}$  over  $S$  can be expressed as:

$$Avg = \frac{1}{A_S} \int_S \left( \frac{K_s + K_c}{8\|\nabla T\|_2^2} \right) dS \quad (4)$$

where  $A_S$  is the area of  $S$  and  $dS$  is the area element. The global fluctuations of the  $\frac{K_s + K_c}{8\|\nabla T\|_2^2}$  around  $Avg$  can be evaluated using the following symmetric energy function:

$$E_w = \int_S \left( \frac{K_s + K_c}{8\|\nabla T\|_2^2} + \frac{8\|\nabla T\|_2^2}{K_s + K_c} \right) dS \quad (5)$$

The discrete form of Equation (5) on a triangular mesh is as follows:

$$E_w = \sum_{i \in |F|} A_i \left( \frac{K_s(A_i) + K_c}{8\|\nabla T(A_i)\|_2^2} + \frac{8\|\nabla T(A_i)\|_2^2}{K_s(A_i) + K_c} \right) \quad (6)$$

where  $F$  denotes the set of triangular mesh faces, and  $|\cdot|$  represents the key map of the set elements. For  $i \in |F|$ ,  $A_i$  denotes the area of the  $i$ -th mesh face; and  $\nabla T(A_i)$  and  $K_s(A_i)$  represent the scalar-field gradient and the discrete curvature along the gradient direction on the corresponding triangular face, respectively. The discrete curvature  $K_s(A_i)$  can be determined as:

$$K_s(A_i) = \left( \frac{\nabla T(A_i)^T}{\|\nabla T(A_i)\|} \right) C_T \left( \frac{\nabla T(A_i)}{\|\nabla T(A_i)\|} \right) \quad (7)$$

where  $C_T$  denotes the curvature tensor on the mesh face, which can be computed following reference [Rusinkiewicz 2004]. Moreover, the sum-of-squares function proposed by Zou et al. [2014] can be adopted to evaluate scallop-height uniformity by approximating the scallop height through scalar-field differences between adjacent machining points. Compared with the sum-of-squares formulation, Equation (6) imposes a stronger penalty as the gradient  $\|\nabla T(A_i)\|$  approaches zero, which helps prevent excessively dense toolpaths.

Subsequently, the fairness of the toolpaths was evaluated. The smoothness of an iso-level curve  $CL$  of the scalar field  $T$  can be quantified by the surface integral of its squared curvature:

$$E_k = \int_S K_f^2 dS \quad (8)$$

where  $K_f$  is the curvature of the iso-level curve  $CL$ , which can be decomposed into two components along the unit orthogonal vectors. The normal curvature vector  $\vec{n}_n$  and the geodesic curvature vector  $\vec{n}_g$  are denoted as  $K_n$  and  $K_g$ , respectively. The relationship between these components is expressed as follows:

$$K_f^2 \vec{n}_f = K_n^2 \vec{n}_n + K_g^2 \vec{n}_g \quad (9)$$

where  $\vec{n}_n$  and  $\vec{n}_g$  are perpendicular to and lie within the tangent plane of  $S$ , respectively. The relationships among  $K_f$ ,  $K_g$ , and  $K_n$  are illustrated in Figures 2(a), 2(c), and 2(d), respectively. Based on this, Equation (8) can be expressed as:

$$E_k = E_n + E_g = \int_S K_n^2 dS + \int_S K_g^2 dS \quad (10)$$

The discrete form of  $E_n$  can be expressed as:

$$E_n = \sum_{i \in |F|} A_i \left( \frac{\nabla T(A_i)}{\|\nabla T(A_i)\|} \right)^T C_T \left( \frac{\nabla T(A_i)}{\|\nabla T(A_i)\|} \right) \quad (11)$$

The discrete form of  $E_g$  can be expressed as:

$$E_g = \sum_{j \in |V|} C_j \operatorname{div} \left( \frac{\nabla T(C_j)}{\|\nabla T(C_j)\|} \right) \quad (12)$$

where  $V$  denotes the set of mesh vertices;  $C_j$  represents the area of the dual cell corresponding to vertex  $j$  for  $j \in V$ ; and  $\operatorname{div} \left( \frac{\nabla T(C_j)}{\|\nabla T(C_j)\|} \right)$  is the divergence of the scalar field at the vertex, which can be computed as follows:

$$\operatorname{div} \left( \frac{\nabla T(C_j)}{\|\nabla T(C_j)\|} \right) = \frac{1}{2C_j} \sum_{k \in F(j)} \frac{\cot \theta_k^1 (e_k^1 \cdot \nabla T(C_k)) + \cot \theta_k^2 (e_k^2 \cdot \nabla T(C_k))}{\nabla T(C_k)} \quad (13)$$

where  $F(j)$  denotes the set of all triangular faces containing vertex  $j$ . The relationships among  $\theta_k^1$ ,  $\theta_k^2$ ,  $e_k^1$ , and  $e_k^2$  on the  $k$ -th triangular face are illustrated in Figure 3.

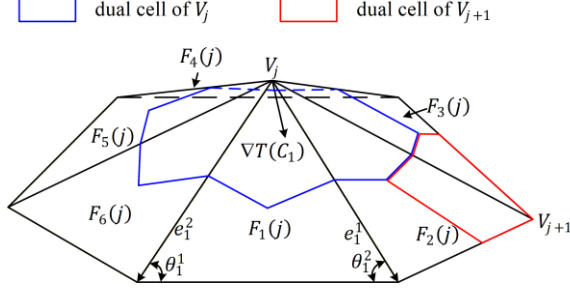


Figure 3: Dual cells of the vertices and the relationships among  $\nabla T$ ,  $\theta_k^1$ ,  $\theta_k^2$ ,  $e_k^1$ , and  $e_k^2$  on the triangular faces.

A comprehensive metric  $E$  is defined to jointly evaluate milling scallop-height uniformity and toolpath smoothness as follows:

$$E = E_w + \alpha E_k \quad (14)$$

where  $\alpha$  is a trajectory scallop uniformity-smoothing weighting parameter selected according to the specific machining conditions.

## 2.2 Scale Field Initialization Based on Conformal Slit Mapping

As shown in Figure 4(a), let the boundaries of a multiply connected surface  $S$  with  $m + 1$  ( $m > 1$ ) edges be denoted as  $\Gamma = \Gamma_0 + \Gamma_1 + \Gamma_2 + \dots + \Gamma_m$ . An initial scalar field  $T_{init}$  is constructed based on conformal slit mapping to approximate the optimal solution of  $T$ .  $T_{init}$  satisfies  $\|\nabla T_{init}\| > 0$  on the open domain  $S \setminus \Gamma$ , and  $T_{init}(\Gamma_i) = C_i$  for  $i = 0, 1, \dots, m$ , where  $C_i$  are the undetermined constants. These conditions ensure that the level sets of  $T_{init}$  strictly conform to the surface boundaries  $\Gamma$  and remain free of self-intersections. The scalar field  $T$  can then be iteratively optimized within the feasible domain while preserving these properties.

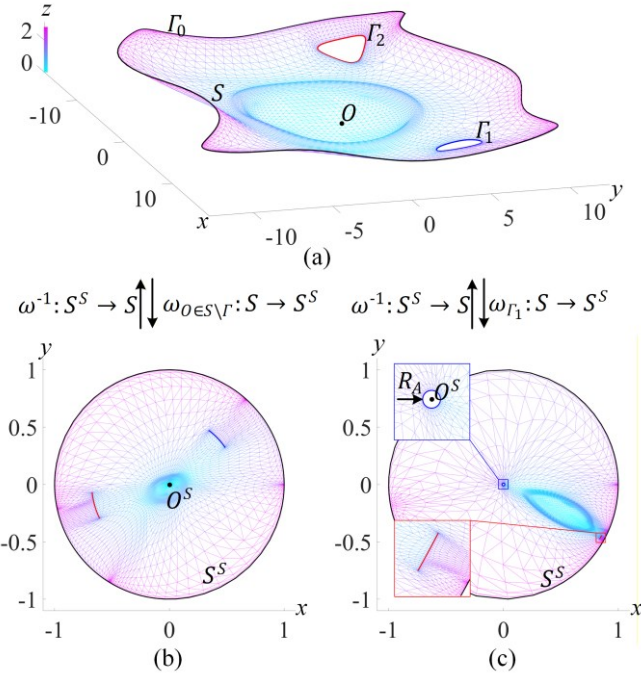


Figure 4: Two types of conformal slit mapping. (a) Original surface, (b) disk conformal slit mapping result, and (c) annular conformal slit mapping result.

The construction of  $T_{init}$  is described as follows:

If a boundary  $\Gamma_0$  and a point  $O \in S \setminus \Gamma$  are selected, a disk conformal mapping can be used to transform  $S$  into a unit disk domain  $D^S$  containing circular arcs. Under this mapping,  $\Gamma_0$  is mapped to the outer boundary of the disk,  $O$  is mapped to the disk center  $O^S$ , and the remaining boundaries  $\Gamma_i$  ( $i = 1, \dots, m$ ) are mapped to arc-shaped slits. If two boundaries of  $S$ , including  $\Gamma_0$  and  $\Gamma_1$ , are designated, an annular conformal mapping transforms  $S$  into a unit annular domain  $A^S$  with circular arcs. In this case,  $\Gamma_0$  is mapped to the outer boundary of the annulus,  $\Gamma_1$  to the inner boundary with radius  $R_A \in (0, 1)$ , and the remaining boundaries  $\Gamma_i$  ( $i = 2, \dots, m$ ) to arc-shaped slits.

In this study, only the most common case of semi-open surfaces was considered. Therefore,  $\Gamma_0$  was fixed as the longest boundary. For convenience, both disk and annular mappings were uniformly denoted as  $\omega$ , and the corresponding mapped domain was denoted as  $S^S$ , expressed as:

$$\begin{cases} \omega_{O \in S \setminus \Gamma}: S \rightarrow S^S \text{ for disk conformal map} \\ \omega_{\Gamma_i, i=1,2,\dots,m}: S \rightarrow S^S \text{ for annular conformal map} \end{cases} \quad (15)$$

The scalar field  $T^S$  on  $S^S$  is defined as follows:

$$T^S = f(\|S^S\|) \quad (16)$$

where  $\|S^S\|$  represents the distance from each element in  $S^S$  to  $O^S$ ; and  $f$  is a monotonically increasing function defined over the interval  $[\min(\|S^S\|), 1]$ , which can be expressed as follows:

$$f: [\min(\|S^S\|), 1] \rightarrow \mathbb{R}, f'(x) > 0 \text{ for } x \in [\min(\|S^S\|), 1] \quad (17)$$

For disk conformal mapping,  $\min(\|S^S\|) = 0$ , whereas for annular conformal mapping,  $\min(\|S^S\|) = R_A$ .

Because  $S^S$  and  $S$  are topologically equivalent, the scalar field  $T^S$  on  $S^S$  can be equivalently mapped back onto  $S$  to obtain  $T$ . Consequently, the scalar field  $T$  on  $S$  is determined by the unknown function  $f$  and an element  $\theta$ , where  $\theta \in \{S - \Gamma\} \cup \{\Gamma_i, i = 1, 2, \dots, m\}$ . Combining this with Equation (14) yields the following equation:

$$\begin{cases} T(\theta, f): S \rightarrow \mathbb{R} \\ E: \{T\} \rightarrow \mathbb{R}^+ \end{cases} \quad (18)$$

Given  $\theta$ , the next objective is to determine a function  $f_{min}$  to minimize  $E$ :

$$\begin{cases} E_{min}(\theta):= \min_{f_{min} \in \{f\}} E(T(\theta, f)) \\ f_{min}(\theta):= \operatorname{argmin}_f E(T(\theta, f)) \end{cases} \quad (19)$$

where  $\{T\}$  and  $\{f\}$  denote the sets of scalar fields  $T$  and functions  $f$  that satisfy the prescribed constraints, respectively. The optimal  $f_{min}$  and the corresponding minimum energy  $E_{min}$  are obtained numerically using a perturbation-based approach. In this approach,  $f$  is represented by a linear interpolation of discrete nodes, with the first node  $f(\min(\|S^S\|))$  fixed. For the remaining nodes, a perturbation  $\delta f$  is introduced at each iteration to preserve  $f' > 0$  while reducing the energy  $E$ , until  $f$  converges to  $f_{min}$  (Figure 5). The detailed implementation is provided in Appendix C of [Shen, Xu, Zhang, Yan and Ding 2025] and is therefore not repeated in this paper.

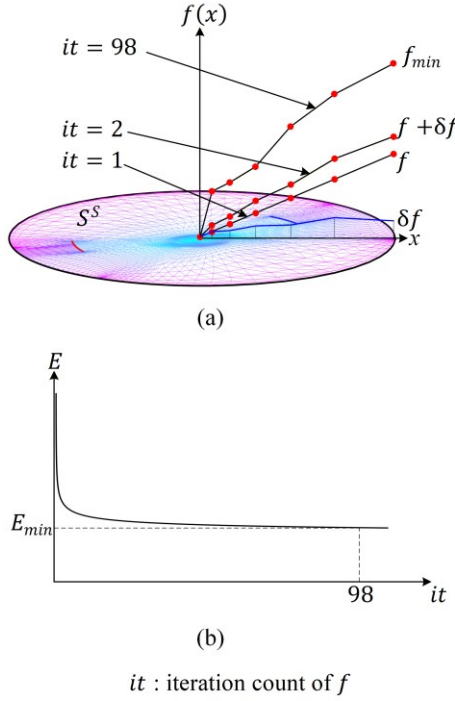


Figure 5: (a) Linearized discretization and iterative refinement of the unknown function  $f$ . (b) Variation in the evaluation metric  $E$  with respect to  $f$  iterations.

Next, the optimal  $\theta$  needs to be determined to minimize  $E_{min}$ :

$$\begin{cases} E_{min}^{opt} := \min_{\theta \in \{S - \Gamma\} \cup \{\Gamma_i, i=1,2,\dots,m\}} E_{min} \\ \theta^{opt} := \operatorname{argmin}_{\theta \in \{S - \Gamma\} \cup \{\Gamma_i, i=1,2,\dots,m\}} E_{min} \end{cases} \quad (20)$$

As illustrated in Figure 6, the optimal element  $\theta^{opt}$  is obtained through a gradient-descent search. Starting from an arbitrary initial point  $\theta_{init}^{opt}$  on  $S \setminus \Gamma$ ,  $\theta^{opt}$  is iteratively updated along the direction of  $\nabla E_{min}$ . When  $\theta$  crosses  $\Gamma_i$  and leaves  $S$  during the search, the gradient  $\nabla E_{min}$  becomes undefined. In such cases,  $\theta$  is transferred to  $\theta_i^{off}$  to allow the iteration to continue, where  $\theta_i^{off}$  is defined as:

$$\theta_i^{off} := \min_{\theta \in \Gamma_i^{off}} E_{min} \quad (21)$$

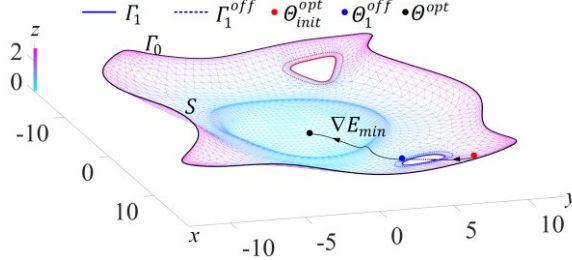


Figure 6: Gradient descent search for  $\theta^{opt}$ .

where  $\Gamma_i^{off}$  represents a curve obtained by offsetting  $\Gamma_i$  slightly towards the interior of surface  $S$ . In this manner, for a given surface  $S$ ,  $\theta^{opt}$  and the corresponding optimal function  $f_{min}$  can be determined such that  $E_{min}^{opt} = E(\theta^{opt}, f_{min})$ . Consequently,  $T(\theta^{opt}, f_{min})$  serves as the desired initial scalar field  $T_{init}$ .

### 2.3 Variational Optimization Method for Scalar-Field Level-Set Toolpaths

As discussed in Section 2.2,  $E(T_{init}) = E_{min}^{opt}$ . However,  $T_{init}$  does not globally minimize  $E$ , and the level-set trajectories derived from  $T_{init}$  therefore admit further improvement. Starting from  $T_{init}$ , the optimal scalar field  $T_{opt}$  minimizing  $E$  is determined by:

$$\begin{cases} E_{opt} := \min_{T \in \{\|\nabla T\| > 0 \text{ on } S \setminus \Gamma, T(\Gamma_i) = C_i \text{ for } i = 0, 1, \dots, m\}} E \\ T_{opt} := \operatorname{argmin}_{T \in \{\|\nabla(T)\| > 0 \text{ on } S \setminus \Gamma, T(\Gamma_i) = C_i \text{ for } i = 0, 1, \dots, m\}} E \end{cases} \quad (22)$$

The procedure is as follows. Let the initial value of  $T$  be  $T_{init}$ . A suitable perturbation  $\delta T$  is then determined such that  $E(T + \delta T) < E(T)$ , while ensuring that  $T + \delta T$  continues to satisfy the imposed constraints:

$$\|\nabla(T + \delta T)\| > 0 \text{ on } S \setminus \Gamma, (T + \delta T)(\Gamma_i) = C_i + \delta C_i \text{ for } i = 0, 1, \dots, m \quad (23)$$

By repeatedly replacing  $T$  with  $T + \delta T$ , the scalar field  $T$  iteratively converges to the optimal solution  $T_{opt}$ .

#### 2.3.1 Scalar-Field Iterative Constraints Derived from Mesh Topology

Based on the topological homeomorphism [Shen et al. 2016] between  $S$  and  $S^S$ , the initial scalar field  $T_{init}$  on  $S$  can be transferred to  $S^S$  to obtain  $T_{init}^S$ . As shown in Figures 7(a) and 7(b), the 2D domain  $S^S$  is then mapped via the homeomorphism  $\omega_H$  to a new slit-containing disk or annular domain, denoted as  $S^H$ :

$$\omega_H: S^S \rightarrow S^H, S_i^H = \frac{S_i^S}{\|S_i^S\|} T_{init}^S(S_i^S) \text{ for } S_i^S \in S^S \quad (24)$$

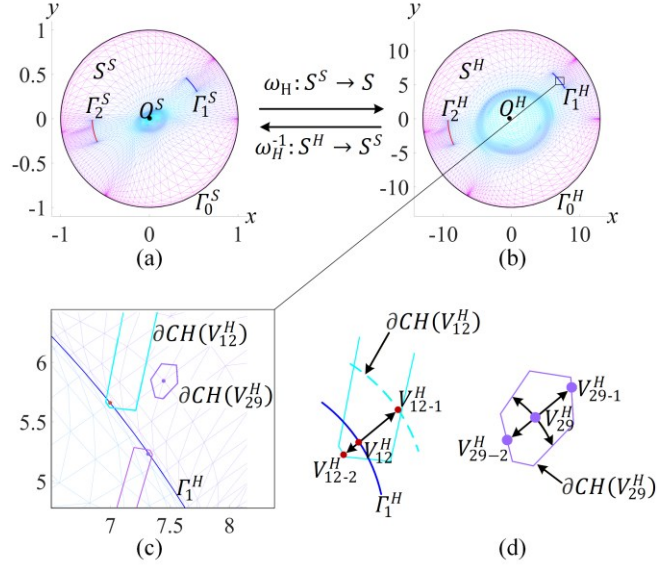


Figure 7: Mesh initialization and iterative constraints. (a) Conformal slit mapping mesh, (b) initialized mesh, (c) convex hull corresponding to vertices, and (d) iterative constraints of vertices corresponding to the convex hull.

The scalar field  $T^H$  defined on  $S^H$  is given by:

$$T^H = \|S^H\| \quad (25)$$

where the scalar value of an element on  $S^H$  represents the distance to the central point  $O^H$ . Because  $S^H$  is topologically equivalent to  $S$ , the scalar field  $T^H$  on  $S^H$  can be transferred back to  $S$  to obtain the scalar field  $T$ . In this manner, the iteration of  $T + \delta T$  is equivalently transformed into an iteration on  $S^H$ , whose initial configuration is specified by Equation (24).

As illustrated in Figure 7(c),  $S^H$  is represented as a discrete triangular mesh, where  $V^H$  and  $F^H$  denote the sets of vertices and faces, respectively. Therefore, the iterative process on  $S^H$  can be described by the motion of  $V^H$ . Consequently, the iterative constraints specified in Equation (23) can be reformulated as two topology-related constraints defined on the mesh of  $S^H$ :

**Constraint 1.** During the iteration on  $S^H$ , the mesh topology should remain homeomorphic to that of  $S$ ; that is, no triangular face in  $S^H$  is allowed to be inverted. This condition ensures that  $\|\nabla(T)\| > 0$  on  $S - \Gamma$ .

**Constraint 2.** Each boundary  $\Gamma_i^H$  should maintain a circular arc shape with center at  $O$ , where  $\Gamma_i^H = \omega_H(\omega(\Gamma_i))$ . This condition ensures that  $T(\Gamma_i) = T^H(\Gamma_i^H) = \|\Gamma_i^H\| = C_i$  for  $i = 0, 1, \dots, m$ .

As shown in Figure 7(d), each vertex  $V_i^H \in V^H$  has two freedom degrees, which correspond to the directions along the meridian and the parallel of  $S^H$ . According to Equation (25), only motion of  $V_i^H$  along the meridian direction affects  $T^H$ , whereas the motion along the parallel direction can only affect the conformal energy of the mapping  $S \rightarrow S^H$ . However, during the iteration on  $S^H$ , a large number of elongated triangular faces may appear, which can lead to numerical overflow when computing the conformal energy and cause instability in the iteration. Moreover, optimizing the motion of  $V_i^H$  along the parallel direction has a negligible effect on the final toolpath planning. Therefore, only the optimization of  $V_i^H$  along the meridian direction was considered. One way to enforce Constraints 1 and 2 is as follows.

**Constraint 1.** Let  $N^1(V_i^H)$  denote the one-ring neighborhood of the mesh vertex  $V_i^H$ . Each triangle within  $N^1(V_i^H)$  exhibits two angles not at  $V_i^H$ , whose angle bisectors on the side containing  $V_i^H$  form a convex hull  $CH(V_i^H)$ . The boundary of this convex hull is denoted as  $\partial CH(V_i^H)$  (Figures 7(c) and (d)). If  $V_i^H$  moves within the open interval  $CH(V_i^H) \setminus \partial CH(V_i^H)$  during each iteration, its motion will not cause any triangle inversion.

**Constraint 2.** All vertices on the same boundary  $\Gamma_i^H$  should move consistently along the radial direction during each iteration.

### 2.3.2 Variational Optimization of Level Set Trajectories under Iterative Constraints

Our objective is to determine  $T_{opt}$  in Equation (22). As described in Section 2.3.1, this problem can be transformed into finding the optimal positions of the vertex set  $V^H$  on the discrete mesh  $S^H$ .

The scalar value  $T(V)$  corresponding to each vertex  $V$  on the discrete mesh  $S$  is given by:

$$T(V) = \|V^H\| \quad (26)$$

The scalar values at other locations on  $S$  are obtained using triangular barycentric interpolation. Let  $N^2(p)$  denote the local mesh formed by the two-ring neighbors of node  $p$ , where  $N^2(p) \in S$ . The local metric value denoted as  $E(N^2(p))$  corresponding to this mesh can still be computed using Equation (14). For any vertex  $V_i^H \in V^H$ , when it moves by a small distance  $\partial V_i^H$  along the radial direction  $\overrightarrow{V_i^H}$ , only the energy on the local mesh  $N^2(V_i^H)$  is affected. Hence,

$$\frac{\partial E}{\partial V_i^H} = \frac{\partial E(N^2(V_i^H))}{\partial V_i^H} \quad (27)$$

where  $\frac{\partial E}{\partial V_i^H}$  indicates whether moving  $V_i^H$  along the radial direction  $\overrightarrow{V_i^H}$ , either forward or backward, will decrease  $E$ . Owing to Constraint 2, all vertices on the same boundary  $\Gamma_i^H$  should move synchronously, either collectively towards or away from the circle center. The corresponding variation of  $E$  caused by the synchronous iterative movement of boundary  $\Gamma_i^H$  can be expressed as:

$$\frac{\partial E}{\partial \Gamma_i^H} = \sum_{j \in |\Gamma_i^H|} \frac{\partial E}{\partial V_j^H}, \text{ where } i = 1, 2, \dots, m \quad (28)$$

By combining Equations (27) and (28), the gradient set  $G^H$  can be expressed as:

$$G^H = \left\{ \frac{\partial E}{\partial V_i^H} \mid i \in |V^H \setminus \Gamma^H| \right\} \cup \left\{ \frac{\partial E}{\partial \Gamma_j^H} \mid j = 1, 2, \dots, m \right\} \quad (29)$$

As illustrated in Figures 7(c) and 7(d), for a vertex  $V_i^H \in V^H \setminus \Gamma^H$  that is not located on the boundary  $\Gamma^H$ , the corresponding convex hull  $CH(V_i^H)$  is bounded. For a vertex  $V_i^H \in \Gamma^H$  located on the boundary, the corresponding convex hull  $CH(V_i^H)$  may be either bounded or unbounded. However, introducing a circular-arc boundary to  $CH(V_i^H)$  (Figure 7(d)) ensures that it becomes bounded, thereby preventing the excessive displacement of boundary vertices during iteration and improving numerical stability. For simplicity, the convex hull with an added circular-arc boundary is denoted as  $CH(V_i^H)$ .

The meridian line passing through  $V_i^H$  intersects the boundary  $\partial CH(V_i^H)$  at two points. The point farther from the center  $O^H$  is denoted as  $V_{i-1}^H$ , and the other point is denoted as  $V_{i-2}^H$ . Accordingly, we define  $\lambda_i^1 = \|\overrightarrow{V_i^H V_{i-1}^H}\|$  and  $\lambda_i^2 = -\|\overrightarrow{V_i^H V_{i-2}^H}\|$ . To prevent mesh inversion, the iteration of each  $V_i^H \in V^H \setminus \Gamma^H$  should satisfy:

$$V_i^H = V_i^H + \lambda_i \frac{V_i^H}{\|V_i^H\|}, \text{ where } \lambda_i \in (\lambda_i^2, \lambda_i^1), i \in |V^H \setminus \Gamma^H| \quad (30)$$

For the set of vertices on the boundary  $\Gamma_i^H$ , where  $i = 1, 2, \dots, m$ , their synchronous iteration is subject to a more stringent constraint:

$$\Gamma_i^H = \Gamma_i^H + \lambda_j \frac{\Gamma_i^H}{\|\Gamma_i^H\|}, \text{ where } \lambda_j \in \left( \lambda_j^2 = \max \left( \lambda_j^2 \Big|_{\Gamma_i^H} \right), \lambda_j^1 = \min \left( \lambda_j^1 \Big|_{\Gamma_i^H} \right) \right) \quad (31)$$

Here,  $\lambda_j^1$  and  $\lambda_j^2$  denote the sets of  $\lambda_j^1$  and  $\lambda_j^2$ , respectively, for all  $j \in |\Gamma_i^H|$ .

For any  $G_i^H$  with  $i \in |G^H|$ , a corresponding feasible interval  $[\lambda_i^1, \lambda_i^2]$  can be obtained by combining Equations (30) and (31). The gradient set  $G^H$  is then normalized within feasible intervals using the following procedure:

$$\begin{cases} G^{H1} = \left\{ \frac{-G_i^H}{\|(1-I_i)\lambda_i^1 + I_i\lambda_i^2\|}, i \in |G^H| \right\} \\ I_i = 0 \text{ for } G_i^H < 0, I_i = 1 \text{ for } G_i^H > 0 \\ G^{H2} = \log \left( \frac{1}{C} - 1 \right) \frac{G^{H1}}{\max(\|G^{H1}\|)}, C \in (0.5, 1) \\ \lambda = \left( \frac{2}{1+e^{G^{H2}}} - 1 \right) \|(1-I_i)\lambda_i^1 + I_i\lambda_i^2\| \end{cases} \quad (32)$$

where  $G^{H1}$  represents the ratio between the energy gradient and the feasible movement range, and  $C \in (0.5, 1)$  is a constant. Larger values of  $C$  lead to faster but less accurate convergence, whereas a value of 0.9 has been observed to perform well across all test cases. By substituting  $\lambda$  from Equation (32) into Equations (30) and (31), a variational iteration process satisfying the required constraints can be obtained.

### 3 EXPERIMENT AND ANALYSIS

#### 3.1 Numerical arithmetic experiments

**Effectiveness analysis of mesh initialization:** The algorithm was run on a desktop with an Intel Core i5-10400F CPU and a Nvidia 1600 GPU. Figures 8(a)–8(c) and 8(f)–8(h) show the mesh iteration processes starting from initialized  $S^H$  and uninitialized  $S^S$ , respectively, whereas Figures 8(d), 8(i), 8(e), and 8(j) illustrate the corresponding iso-paths before and after iterations. By comparing Figure 8(e) with Figure 8(j), the converged trajectories are nearly identical. However, initializing the process with  $S^H$  reduced the convergence time by 23.42%, decreasing from 1273.62 to 298.24 s. This indicated that the proposed initialization effectively reduced both the number of iterations and the overall computation time without introducing any noticeable influence on the final trajectory. The underlying reasons could be as follows:

1. Although the trajectories corresponding to the isoparametric curves of  $S^H$  and  $S^S$  exhibited similar overall shapes, the initial states shown in Figures 8(a) and 8(b) revealed an evident difference. In particular, in regions near the center, where conformal mapping introduced severe radial distance distortion [Xu et al. 2019], the trajectory spacing generated from the  $S^H$  isoparametric curves was noticeably more uniform than that generated from  $S^S$ . As a result, fewer iterations are required to achieve uniform spacing during the optimization process.
2. The key step in transforming  $S^S$  into  $S^H$  was the  $f_{min}$  operation defined in Equation (19), whose computational complexity was  $O \left( N_F \log \left( \frac{1}{E_\epsilon^S} \right) \right)$ , where  $N_F$  denotes the number of triangular faces of  $S$  and  $E_\epsilon^S$  is the convergence energy threshold. This procedure has been demonstrated to be efficient in a previous study [Shen et al. 2025] and requires only 1.73 s in the test case. Therefore, it is reasonable to invest a small amount of additional computation time in mesh initialization to achieve a substantial reduction in the overall optimization costs.

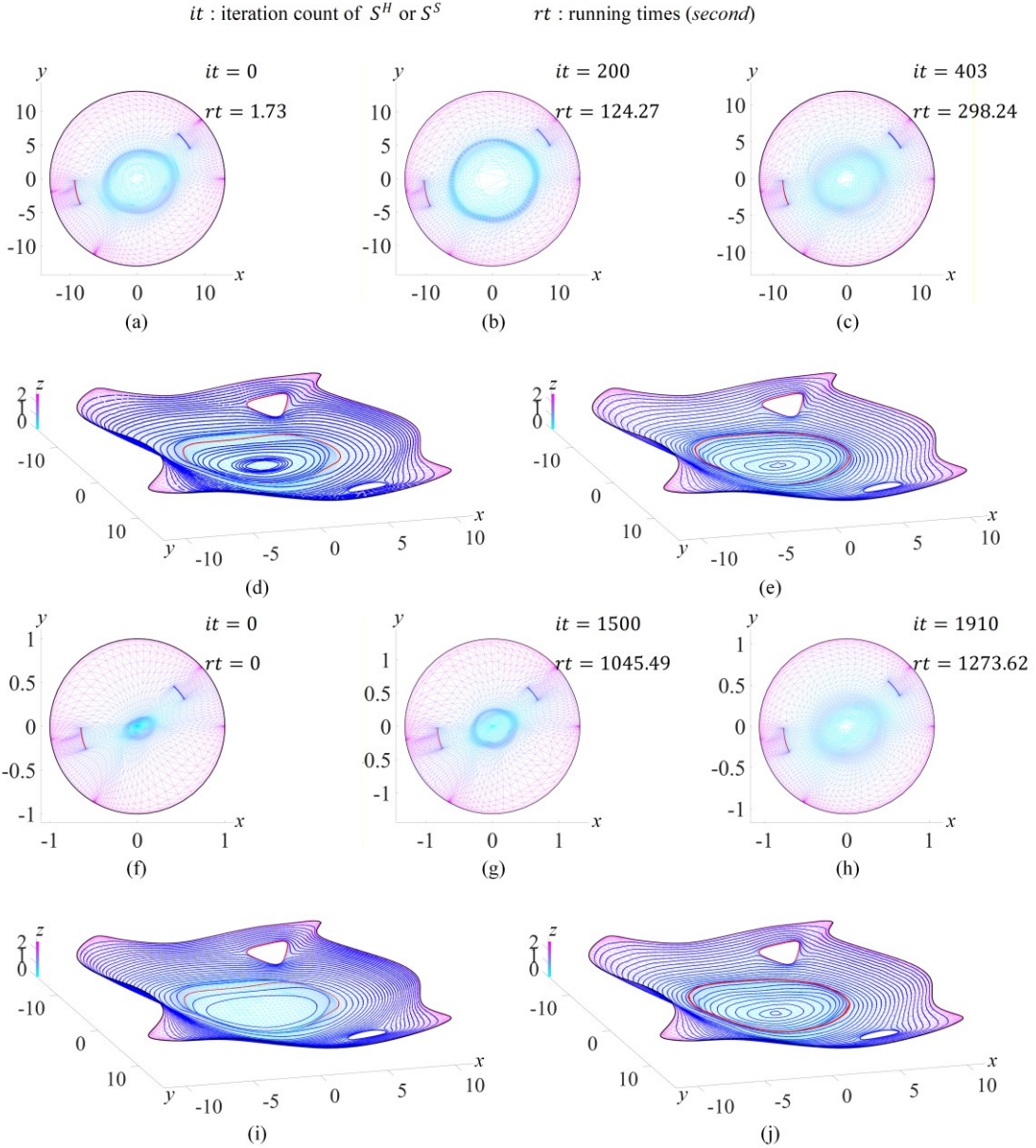


Figure 8: Variational iteration process of the mesh. (a)  $S^H$  mesh obtained from the initialization of  $S^S$ ; (b)  $S^H$  mesh during iteration; (c) converged  $S^H$  mesh; (d) iso-paths of the initialized  $S^H$  mesh; (e) iso-paths of the converged  $S^H$  mesh; (f) uninitialized  $S^S$  mesh; (g)  $S^S$  mesh during iteration; (h) converged  $S^S$  mesh; (i) iso-paths of the uninitialized  $S^S$  mesh; (j) iso-paths of the converged  $S^S$  mesh.

Notably, a difference was observed between the red trajectories in Figures 8(d) and 8(e). The optimized trajectory aligned more closely with the low-curvature direction of the boss feature than the trajectory generated directly from conformal slit mapping. This alignment can help avoid frequent crossings over the boss, thereby reducing abrupt directional changes in the toolpath.

**Effect of the weighting parameter  $\alpha$ :** Figures 9(a)–9(c) illustrate the differences among tool contact trajectories generated using different values of the weighting parameter  $\alpha$  in Equation (14), with the prescribed machining scallop height  $h_{set}$  fixed at 0.2. Figure 9(d) shows the trajectory generated using the conformal slit mapping method [Shen et al. 2025], with the origin mapped point  $\theta$  set to be the same as that in Figure 9(b); this result was used as the reference. Figure 9(e) compares the generated tool contact trajectories in terms of total path length  $|L|$ , turning smoothness index  $\overline{\rho^2}$ , machining redundancy index  $\overline{CT^2}$ , and the maximum repetition coverage count  $\max(CT)$ . The trajectory smoothness index  $\overline{\rho^2}$  is defined as:

$$\overline{\rho^2} = \int_L \rho^2 dL \quad (33)$$

where  $dL$  represents the differential element of the tool-contact trajectory  $L$ , and  $\rho$  is the curvature corresponding to each differential segment. The squared curvature term  $\rho^2$  imposes a larger penalty on high-curvature regions, and a smaller value of the smoothness metric  $\overline{\rho^2}$  indicates a smoother trajectory.

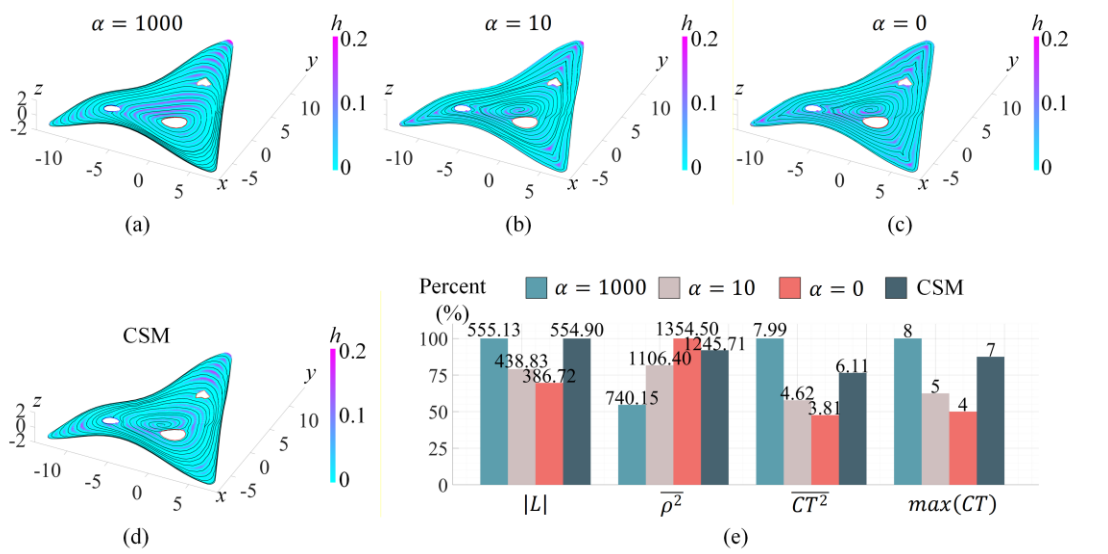


Figure 9: Tool contact trajectories and evaluation metrics: (a)–(c) effect of weighting parameter  $\alpha$ ; (d) conformal slit mapping method (reference); (e) multi-indicator comparison.

The machining redundancy index  $\overline{CT^2}$  is defined as follows:

$$\overline{CT^2} = \int_{S^h} CT^2 ds \quad (34)$$

where  $S^h$  denotes the iso-scallop-height surface obtained by offsetting the original surface  $S$  along the normal direction by the prescribed scallop height  $h_{set}$ ,  $ds$  represents a differential element of  $S^h$ , and  $CT$  indicates the number of times a differential element is covered by different trajectories (Figure 10). By adopting the squared term of  $CT$ , regions with multiple redundant coverage were penalized more heavily. A smaller value of the redundancy metric  $\overline{CT^2}$  indicated less redundant machining, and a smaller maximum repetition count  $\max(CT)$  corresponded to reduced trajectory redundancy.

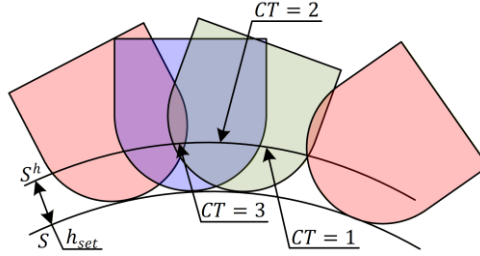
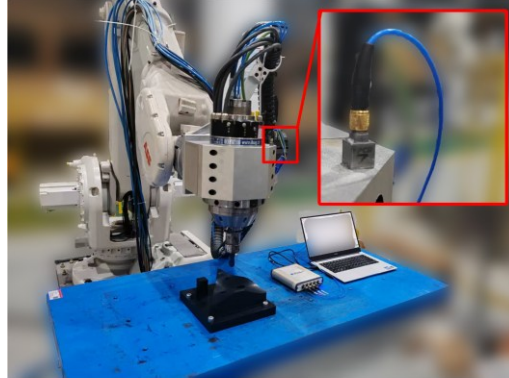


Figure 10: Cross-sectional view of the coverage of iso-scallop-height surfaces by adjacent tool positions.

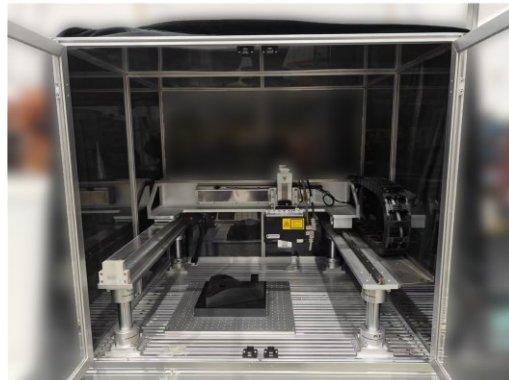
As shown in Figure 9(e), as the smoothness weighting parameter  $\alpha$  decreased, the metrics  $|L|$ ,  $\overline{CT^2}$ , and  $\max(CT)$  decreased simultaneously, demonstrating the reduced trajectory redundancy as well as more consistent spacing and scallop height. Furthermore, the smoothness metric  $\overline{\rho^2}$  increased, implying a reduction in trajectory smoothness. Therefore,  $\alpha$  can be adjusted according to specific requirements, where a smaller  $\alpha$  favors shorter trajectories with more uniform scallop height, whereas a larger  $\alpha$  favors trajectories with smoother directional transitions. When  $\alpha = 10$ , the resulting trajectory achieved uniformly better values across all metrics than the trajectory generated using conformal slit mapping, further confirming the effectiveness of the proposed method.

### 3.2 Experiment on surface milling

An experimental comparison was conducted to evaluate the machining performance of two trajectories: Path 1 generated by the proposed algorithm with  $\alpha = 10$ , and Path 2 generated using the conformal slit mapping method [Shen et al. 2025]. Figure 11(a) shows the IRB6600 robotic milling system, in which a PCB triaxial accelerometer was mounted on the spindle to measure the dynamic cutting vibrations at a sampling frequency of 2000 Hz. Figure 11(b) shows the three-coordinate laser measurement system for surface inspection, which provided a measurement accuracy of 20  $\mu\text{m}$ .



(a)



(b)

Figure 11: Experimental setup. (a) IRB6600 robotic milling system equipped with a PCB triaxial accelerometer and (b) three-coordinate laser measurement system.

All non-critical control variables are summarized in Table 1 and were kept constant to ensure a fair and unbiased comparison.

Table 1. Machining performance metrics under identical control conditions.

Variable	Tool radius (mm)	Number of flutes	Tool overhang length (mm)	Spiral motion direction	Axial depth of cut (mm)	Spindle speed (rpm)	Workpiece material
value	10	2	79.2	From inside to outside	4.00	1000	Engineering plastic (ABS)

Figure 12 presents the surface-scanned point clouds and measured spindle acceleration signals from left to right for the machined workpieces, where the upper and lower rows correspond to the experimental results for Path 1 and Path 2, respectively. Except for the prescribed feed rate, all machining parameters were kept identical in the two experiments. As shown in Figures 12(b) and 12(d), the machining scallops of Path 1 and Path 2 closely match the simulation results in Figures 9(b) and 9(d). The maximum machining residuals were 2.24 mm and 2.32 mm (16% deviation from the set value of 2 mm). However, the difference between the two experiments is less than 5%, and the subsequent data exhibit clear and valid features, demonstrating the effectiveness of the experiment.

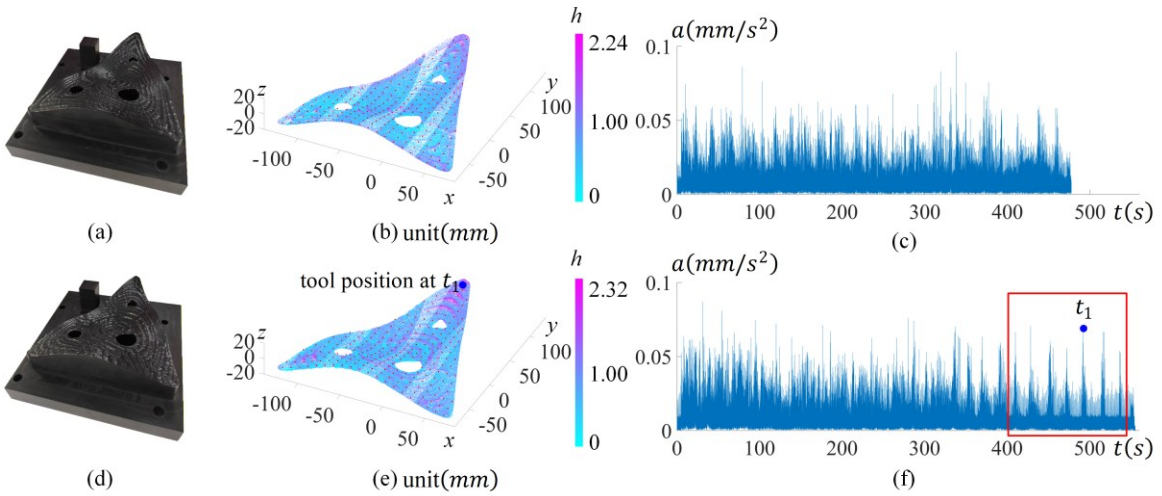


Figure 12: Comparison of experimental results (upper: proposed method; lower: conformal slit mapping), showing (from left to right) machined workpieces, scanned point clouds, and spindle acceleration signals.

Table 2 summarizes the quantitative comparison of machining performance metrics, with the third row presenting the ratio of the metrics for Path 1 to Path 2. Specifically,  $F_R$  denotes the prescribed feed rate, and *time* represents the total machining time; and  $S_C$  is the global scallop height consistency metric defined based on practical part quality inspection procedures. A set of sampling points  $Pt$  was selected on the machined surface, as indicated by the red points in Figures 12(b) and 12(e). For each point  $Pt_i \in Pt$ , the maximum scallop height  $msh(Pt_i)$  was evaluated within a local neighborhood defined as a spherical region centered at  $Pt_i$  with tool radius  $K_c$ . The metric  $S_C$  was defined as the variance of  $msh(Pt_i)$  over all sampling points:

$$S_C = \text{var}(\{Pt_i \in Pt | msh(Pt_i)\}) \quad (35)$$

Table 2: Quantitative comparison of machining performance metrics between Path 1 (proposed method) and Path 2 (conformal slit mapping).

	$F_R$ mm/s	<i>time</i> sec	$S_C$ mm <sup>2</sup> (experiment)	$S_C$ mm <sup>2</sup> (simulation)	$a_{mean}$ $10^{-3} \text{mm/s}^2$	$a_{var}$ $10^{-5} \text{mm}^2/\text{s}^4$	$a_{cu}$ $10^{-1} \text{mm}^2/\text{s}^3$	$a_{tcu}$ $10^{-4} \text{mm}^2/\text{s}^3$
Path 1	10.00	466.33	0.2101	0.2007	9.64	3.53	6.03	6.51
Path 2	11.00	543.75	0.2228	0.2140	9.21	3.98	6.85	8.38
	90.91%	85.76%	94.30%	93.79%	104.67%	88.69%	87.93%	77.38%

In addition,  $a_{mean}$  and  $a_{var}$  denote the mean value and variance of the measured spindle acceleration signal, respectively. The cumulative impact indicator  $a_{cu}$  and the threshold-based cumulative impact indicator  $a_{tcu}$ , defined as the accumulated acceleration exceeding a threshold of  $0.05 \text{mm/s}^2$ , were employed to evaluate the overall and extreme impact loads experienced by the actuator throughout the machining process. They are defined as follows:

$$a_{cu} = \int a^2 dt \quad (36)$$

$$a_{tcu} = \int \text{exceed}T_{0.05}(a^2) dt \quad (37)$$

where

$$\text{exceed}T_{0.05}(a^2) = a^2 \text{ for } a > 0.05 \text{ mm/s}^2, \text{exceed}T_{0.05}(a^2) = 0 \text{ otherwise} \quad (38)$$

The experimental results provide insights into the causal relationships among trajectory characteristics, machining efficiency, scallop height consistency, and process stability. Although both trajectories share identical topological properties, including a single tool entry and exit, an outward spiral motion, and the absence of hole crossing or self-intersection, their geometric organization over the surface leads to substantially different machining responses.

Although the prescribed feed rate of Path 1 ( $F_R = 10 \text{ mm/s}$ ) was 9.09% lower than that of Path 2 ( $F_R = 11 \text{ mm/s}$ ), Path 1 achieved a 14.24% shorter machining time (466.33 s versus 543.75 s). This improvement was primarily attributed to a 20.92% reduction in the path length resulting from the elimination of redundant coverage by the proposed algorithm.

The 5.70% reduction in  $S_C$  obtained for Path 1 demonstrated a more uniform scallop height distribution over the surface, which was consistent with the 6.21% reduction predicted by simulation. This improvement was mainly due to the ability of the proposed method to enforce global regularity in the scallop height distribution along the trajectory.

From a dynamic perspective, Path 1 exhibited a 4.67% increase in the mean spindle acceleration, reflecting a higher average material removal rate. However, machining stability was governed not by the absolute cutting load but by its variation along the trajectory. The consistently lower values of  $a_{var}$ ,  $a_{cu}$ , and  $a_{tcu}$  observed for Path 1 indicated a pronounced reduction in impulsive load fluctuations, with all three indicators reduced by more than 10% (approximately 11%, 12%, and 23%, respectively) compared with Path 2. This behavior can be attributed to the smaller variation in the material removal rate along Path 1.

This effect was particularly evident in the red-highlighted region of Figure 12(f), where the toolpath approached the outer boundary of the workpiece. In this area, the trajectory generated by conformal slit mapping exhibited pronounced acceleration pulses, resulting from abrupt variations in local cutting engagement, especially in corner-dominated regions, where the cutting rate became significantly higher than in adjacent areas. In contrast, the smoother spatial distribution of Path 1 alleviated abrupt engagement transitions, leading to a more uniform and stable dynamic response.

Overall, the experimental results suggest that regulating the trajectory redundancy and local engagement variation through the weighting parameter enables concurrent improvements in machining efficiency, scallop height consistency, and process stability. This unified control mechanism highlights the practical advantages of the proposed trajectory generation method over conformal slit mapping-based approaches for complex freeform surface milling.

## 4 SUMMARY AND OUTLOOK

### 4.1 Summary

This study presented a variational scalar-field framework for multiply connected (porous) freeform surfaces with the aim of achieving two core objectives: (1) the generation of boundary-conforming, continuous, and self-intersection-free spiral toolpaths through topology-preserving mesh deformation, and (2) the simultaneous optimization of global scallop height uniformity and path smoothness via scalar-field variational optimization, in which an adjustable weighting parameter  $\alpha$  was introduced to balance these competing objectives. Compared with conformal slit mapping, the proposed approach improved the machining efficiency by 14.24%, enhanced the scallop height uniformity by 5.70%, and reduced the milling impact by more than 10%.

To guarantee boundary conformity and avoid zero-gradient singularities, the scalar field must satisfy strict interior and boundary constraints. These constraints are reformulated as topology-preserving mesh optimization and boundary co-

circularity enforcement, ensuring their preservation throughout the entire iterative optimization process and effectively preventing boundary nonconformity, discontinuities, and self-intersection of toolpaths.

Furthermore, conformal slit mapping was employed to construct a feasible initial mesh configuration that inherently satisfied both types of constraints. This initialization mitigated numerical instability, suppressed radial distortion induced by conformal mapping, and significantly reduced the required number of iterations and overall computational cost, thereby providing a stable and efficient foundation for subsequent scalar-field optimization.

## 4.2 Outlook

Because the scalar field can be influenced by both its initialization and locally linearized perturbation updates, attaining a globally optimal solution remains challenging. Introducing stochastic exploration into the iterative optimization process may provide a viable means of approaching more globally optimal scalar-field configurations.

In addition, the Riemannian metric derived from scallop height analysis can be replaced with metrics tailored to other domain-specific coverage objectives [Zou 2021], such as additive manufacturing or UAV area coverage. Consequently, the proposed framework exhibits strong potential for extension to a broader class of coverage path planning problems.

## ACKNOWLEDGMENTS

This study was supported by the National Natural Science Foundation of China (52188102, 52375495). We sincerely thank Dr. Yang Zeyuan for valuable comments and insightful suggestions that greatly improved the quality of this manuscript.

## FUNDING

This research received no specific grant from any funding agency in the public, commercial, or not-for-profit sectors.

## DECLARATION OF CONFLICTING INTERESTS

The Authors declare that there is no conflict of interest.

## REFERENCES

Ercan U. Acar, Howie Choset, Yangang Zhang, and Mark Schervish. 2003. Path Planning for Robotic Demining: Robust Sensor-Based Coverage of Unstructured Environments and Probabilistic Methods. *Int. J. Robot. Res.* 22, 7–8 (July 2003), 441–466. <https://doi.org/10.1177/02783649030227002>

Xiaomeng Ban, Mayank Goswami, Wei Zeng, Xianfeng Gu, and Jie Gao. 2013. Topology dependent space filling curves for sensor networks and applications. In *2013 Proceedings IEEE INFOCOM*. IEEE, Turin, Italy, 14–19 April 2013. <https://doi.org/10.1109/INFCOM.2013.6567019>

Michael Bartoň, Michal Bizzarri, Florian Rist, Oleksii Sliusarenko, and Helmut Pottmann. 2021. Geometry and tool motion planning for curvature adapted CNC machining. *ACM Trans. Graph.* 40, 4 (July 2021), 1–16. <https://doi.org/10.1145/3450626.3459837>

E. Bohez, S. S. Makhanov, and K. Sonthipermpoon. 2000. Adaptive nonlinear tool path optimization for five-axis machining. *Int. J. Prod. Res.* 38, 17 (November 2010), 4329–4343. <https://doi.org/10.1080/00207540050205127>

Marcel Campen, Cláudio T. Silva, and Denis Zorin. 2016. Bijective maps from simplicial foliations. *ACM Trans. Graph.* 35, 4 (July 2016), 1–15. <https://doi.org/10.1145/2897824.2925890>

Haokun Chen, Dong He, Jiancheng Hao, Pengcheng Hu, and Kai Tang. 2025. Singularity-free PINN-based path planning method for the table-tilt five-axis machine\*. In *2025 IEEE International Conference on Real-time Computing and Robotics (RCAR)*. IEEE, Toyama, Japan, 636–641. <https://doi.org/10.1109/RCAR65431.2025.11139420>

Zhongwei Chen, Xian Wu, Kai Zeng, Jianyun Shen, Feng Jiang, Zhongyuan Liu, and Wenjun Luo. 2021. Investigation on the Exit Burr Formation in Micro Milling. *Micromachines (Basel)* 12, 8 (August 2021), 952. <https://doi.org/10.3390/mi12080952>

Gary P. T. Choi. 2021. Efficient Conformal Parameterization of Multiply-Connected Surfaces Using Quasi-Conformal Theory. *J. Sci. Comput.* 87, (April 2021), 70. <https://doi.org/10.1007/s10915-021-01479-y>

Francesco Della Santa and Sandra Pieraccini. 2023. Discontinuous neural networks and discontinuity learning. *J. Comput. Appl. Math.* 419, (February 2023), 114678. <https://doi.org/https://doi.org/10.1016/j.cam.2022.114678>

Robson Bruno Dutra Pereira, Gaizka Gómez-Escudero, Amaia Calleja-Ochoa, Haizea González-Barrio, Carlos Henrique Lauro, Lincoln Cardoso Brandão, and Luis Norberto López de Lacalle. 2025. Enhancing productivity of helical milling of Inconel 718 by optimization with constraint learning. *Int. J. Adv.*

*Manuf. Technol.* 138, 2 (April 2025), 783–804. <https://doi.org/10.1007/s00170-025-15574-z>

Neelotpal Dutta, Tianyu Zhang, Guoxin Fang, Ismail E. Yigit, and Charlie C. L. Wang. 2023. Vector Field-Based Volume Peeling for Multi-Axis Machining. *J. Comput. Inf. Sci. Eng.* 24, 5 (May 2024), 051001. <https://doi.org/10.1115/1.4063861>

Zhenghui Ge, Qifan Hu, Ziyi Wang, and Yongwei Zhu. 2024. Spiral tool path generation method for complex pocket machining based on electrostatic field theory. *J. Braz. Soc. Mech. Sci. Eng.* 46, 10 (September 2024), 614. <https://doi.org/10.1007/s40430-024-05191-4>

Fernando de Goes, Mathieu Desbrun, and Yiying Tong. 2016. Vector field processing on triangle meshes. In *Proceedings of the ACM SIGGRAPH 2016 Courses*, Association for Computing Machinery, Anaheim, California, Article 27, 49 pages. <https://doi.org/10.1145/2897826.2927303>

Tamara G. Grossmann, Urszula Julia Komorowska, Jonas Latz, and Carola-Bibiane Schönlieb. 2024. Can physics-informed neural networks beat the finite element method? *IMA J. Appl. Math.* 89, 1 (May 2024), 143–174. <https://doi.org/10.1093/imamat/hxae011>

David Hajdu, Oier Franco, Markel Sanz-Calle, Giovanni Totis, Jokin Munoa, Gabor Stepan, and Zoltan Dombovari. 2025. Stable tongues induced by milling tool runout. *International Journal of Machine Tools and Manufacture* 206, (March 2025), 104258. <https://doi.org/10.1016/j.ijmachtools.2025.104258>

Jiancheng Hao, Haokun Chen, Pengcheng Hu, Dong He, Yamin Li, Xiaoke Deng, Tak Yu Lau, Fan Shi, and Yanglong Lu. 2025. Neural surface partitioner: A physics-informed neural network for five-axis machining by a non-spherical cutting tool. *J. Manuf. Syst.* 83, (December 2025), 976–991. <https://doi.org/10.1016/j.jmsy.2025.11.015>

Martin Held and Stefan de Lorenzo. 2018. On the generation of spiral-like paths within planar shapes. *J. Comput. Des. Eng.* 5, 3 (July 2018), 348–357. <https://doi.org/10.1016/j.jcde.2017.11.011>

Bo H. Kim and Byoung K. Choi. 2002. Machining efficiency comparison direction-parallel tool path with contour-parallel tool path. *Comput.-Aided Des.* 34, 2 (February 2002), 89–95. [https://doi.org/10.1016/S0010-4485\(00\)00139-1](https://doi.org/10.1016/S0010-4485(00)00139-1)

Eungki Lee. 2003. Contour offset approach to spiral toolpath generation with constant scallop height. *Comput.-Aided Des.* 35, 6 (May 2003), 511–518. [https://doi.org/10.1016/S0010-4485\(01\)00185-3](https://doi.org/10.1016/S0010-4485(01)00185-3)

Wan-chiu Li, Bruno Vallet, Nicolas Ray, and Bruno Levy. 2006. Representing Higher-Order Singularities in Vector Fields on Piecewise Linear Surfaces. *IEEE Trans. Vis. Comput. Graph.* 12, 5 (September 2006), 1315–1322. <https://doi.org/10.1109/TVCG.2006.173>

Dongyi Li and Yibin Lu. 2025. A method of numerical conformal mapping of bounded regions with a rectilinear slit. *AIMS Math.* 10, 10 (April 2025), 8422–8445. <https://doi.org/10.3934/math.2025388>

Yu-Yao Lin, Chien-Chun Ni, Na Lei, Xianfeng David Gu, and Jie Gao. 2017. Robot Coverage Path planning for general surfaces using quadratic differentials. In *2017 IEEE International Conference on Robotics and Automation (ICRA)*. IEEE, Singapore, 5005–5011. <https://doi.org/10.1109/ICRA.2017.7989583>

Stanislav S. Makanov. 2022. Vector fields for five-axis machining. A survey. *Int. J. Adv. Manuf. Technol.* 122, (August 2022), 533–575. <https://doi.org/10.1007/s00170-022-09445-0>

Rahul A. Mali, T. V. K. Gupta, and J. Ramkumar. 2021. A comprehensive review of free-form surface milling—Advances over a decade. *J. Manuf. Process.* 62, (February 2021), 132–167. <https://doi.org/10.1016/j.jmapro.2020.12.014>

Felipe Marin, Guillermo González, Luis Norberto López de Lacalle, Naiara Ortega, Gaizka Gómez-Escudero, Pablo Fernández-Lucio, Ander Del Olmo, and Haizea González. 2025. Dimensional errors of aeronautical casings caused by machining of thin walls and features. *Results Eng.* 26, (June 2025), 104719. <https://doi.org/10.1016/j.rineng.2025.104719>

Rahul Mitra, Erick Jimenez Berumen, Megan Hofmann, and Edward Chien. 2024. Singular Foliations for Knit Graph Design. In *Proceedings of the ACM SIGGRAPH 2024 Conference Papers*. Association for Computing Machinery, Denver, CO, USA, Article 38, 11 pages. <https://doi.org/10.1145/3641519.3657487>

Mohamed M. S. Nasser. 2011. Numerical conformal mapping of multiply connected regions onto the second, third and fourth categories of Koebe’s canonical slit domains. *J. Math. Anal. Appl.* 382, 1 (October 2011), 47–56. <https://doi.org/10.1016/j.jmaa.2011.04.030>

Nasim Rahaman, Aristide Baratin, Devansh Arpit, Felix Draxler, Min Lin, Fred Hamprecht, Yoshua Bengio, and Aaron Courville. 2019. On the Spectral Bias of Neural Networks. In *Proceedings of the 36th International Conference on Machine Learning*. PMLR, 5301–5310.

S. Rusinkiewicz. 2004. Estimating curvatures and their derivatives on triangle meshes. In *Proceedings. 2nd International Symposium on 3D Data Processing, Visualization and Transmission*. IEEE, Thessaloniki, Greece, 486–493. <https://doi.org/10.1109/TDPVT.2004.1335277>

Zhengyang Shen, Xu Han, Zhenlin Xu, and Marc Niethammer. 2019. Networks for Joint Affine and Non-parametric Image Registration. In *Proceedings of the IEEE/CVF Conference on Computer Vision and Pattern Recognition (CVPR)*. IEEE, 4224–4233.

Changqing Shen, Sihao Mao, Bingzhou Xu, Ziwei Wang, Xiaojian Zhang, Sijie Yan, and Han Ding. 2024. Spiral complete coverage path planning based on conformal slit mapping in multi-connected domains. *Int. J. Robot. Res.* 43, 14 (May 2024), 2183–2203. <https://doi.org/10.1177/02783649241251385>

Changqing Shen, BingZhou Xu, Xiaojian Zhang, Sijie Yan, and Han Ding. 2025. Conformal Slit Mapping Based Spiral Tool Trajectory Planning for Ball-end Milling on Complex Freeform Surfaces. arXiv:2504.06310. Retrieved from <https://doi.org/10.48550/arXiv.2504.06310>

Junnan Song and Shalabh Gupta. 2018.  $\varepsilon^*$ : An Online Coverage Path Planning Algorithm. *IEEE Trans. Robot.* 34, 2 (April 2018), 526–533. <https://doi.org/10.1109/TRO.2017.2780259>

Yuwen Sun, Jinting Xu, Chunling Jin, and Dongming Guo. 2016. Smooth tool path generation for 5-axis machining of triangular mesh surface with nonzero genus. *Comput.-Aided Des.* 79, (October 2016), 60–74. <https://doi.org/10.1016/j.cad.2016.06.001>

Josh Vekhter, Jiacheng Zhuo, Luisa F Gil Fandino, Qixing Huang, and Etienne Vouga. 2019. Weaving geodesic foliations. *ACM Trans. Graph.* 38, 4 (July 2019), Article 34, 22 pages. <https://doi.org/10.1145/3306346.3323043>

Shu Wang, Hui Zhang, Bingran Li, and Peiqing Ye. 2025. Tool trajectory planning with inter-path consistency of feedrate for freeform surface machining. *CIRP J. Manuf. Sci. Technol.* 62, (November 2025), 1–15. <https://doi.org/10.1016/j.cirpj.2025.08.003>

Chenming Wu, Chengkai Dai, Xiaoxi Gong, Yong-Jin Liu, Jun Wang, Xianfeng David Gu, and Charlie C. L. Wang. 2019. Energy-Efficient Coverage Path Planning for General Terrain Surfaces. *IEEE Robot. Autom. Lett.* 4, 3 (July 2019), 2584–2591. <https://doi.org/10.1109/LRA.2019.289920>

Kang Wu and Yibin Lu. 2023. Numerical computation of preimage domains for spiral slit regions and simulation of flow around bodies. *Math. Biosci. Eng.* 20, 1 (October 2022), 720–736. <https://doi.org/10.3934/mbe.2023033>

Lei Wu, Xizhe Zang, Wenxin Yin, Xuehe Zhang, Changle Li, Yanhe Zhu, and Jie Zhao. 2024. Pose and Path Planning for Industrial Robot Surface Machining Based on Direction Fields. *IEEE Robot. Autom. Lett.* 9, 11 (November 2024), 10455–10462. <https://doi.org/10.1109/LRA.2024.3474521>

Chen-Yang Xu, Jing-Rong Li, Qing-Hui Wang, and Guang-Hua Hu. 2019. Contour parallel tool path planning based on conformal parameterisation utilising mapping stretch factors. *Int. J. Prod. Res.* 57, 1 (March 2018), 1–15. <https://doi.org/10.1080/00207543.2018.1456699>

Xiaohu Xu, Songtao Ye, Zeyuan Yang, Sijie Yan, and Han Ding. 2022. Global optimal trajectory planning of mobile robot grinding for high-speed railway body. In: Honghai Liu, Zhouping Yin, Lianqing Liu, Li Jiang, Guoying Gu, Xinyu Wu, and Weihong Ren. *Intelligent Robotics and Applications. ICIRA 2022*. Springer, Cham. [https://doi.org/10.1007/978-3-031-13835-5\\_44](https://doi.org/10.1007/978-3-031-13835-5_44)

Sijie Yan, Xiaohu Xu, Zeyuan Yang, Dahu Zhu, and Han Ding. 2019. An improved robotic abrasive belt grinding force model considering the effects of cut-in and cut-off. *J. Manuf. Process.* 37, (January 2019), 496–508. <https://doi.org/10.1016/j.jmapro.2018.12.029>

Tong Yang, Jaime Valls Miro, Minh Nguyen, Yue Wang, and Rong Xiong. 2023. Template-Free Nonrevisiting Uniform Coverage Path Planning on Curved Surfaces. *IEEE/ASME Trans. Mechatron.* 28, 4 (August 2023), 1853–1861. <https://doi.org/10.1109/TMECH.2023.3275214>

Zeyuan Yang, Xiaohu Xu, Minxing Kuang, Dahu Zhu, Sijie Yan, Shuzhi Sam Ge, and Han Ding. 2024. Dynamic compliant force control strategy for suppressing vibrations and over-grinding of robotic belt grinding system. *IEEE Transactions on Automation Science and Engineering*. 21, 3 (July 2024), 4536–4547. <https://doi.org/10.1109/TASE.2023.3298357>

Eugene Zhang, Konstantin Mischaikow, and Greg Turk. 2006. Vector field design on surfaces. *ACM Trans. Graph.* 25, 4 (October 2006), 1294–1326. <https://doi.org/10.1145/1183287.1183290>

Tao Zhao, Zhaoyang Yan, Liwei Wang, Rui Pan, Xiaowei Wang, Kun Liu, Kaiwei Guo, Qingsong Hu, and Shujun Chen. 2024. Hybrid path planning method based on skeleton contour partitioning for robotic additive manufacturing. *Robot. Comput.-Integr. Manuf.* 85, (February 2024), 102633. <https://doi.org/10.1016/j.rcim.2023.102633>

Chungang Zhuang, Zhenhua Xiong, and Han Ding. 2010. High speed machining tool path generation for pockets using level sets. *Int. J. Prod. Res.* 48, 19 (October 2010), 5749–5766. <https://doi.org/10.1080/00207540903232771>

Qiang Zou. 2021. Length-optimal tool path planning for freeform surfaces with preferred feed directions based on Poisson formulation. *Comput.-Aided Des.* 139, (October 2021), 103072. <https://doi.org/10.1016/j.cad.2021.103072>

Qiang Zou, Juyong Zhang, Bailin Deng, and Jibin Zhao. 2014. Iso-level tool path planning for free-form surfaces. *Comput.-Aided Des.* 53, (August 2014), 117–125. <https://doi.org/10.1016/j.cad.2014.04.006>